


**ORIGINAL RESEARCH**

# Experimental demonstrations of high-accuracy 3D/2D indoor visible light positioning using imaging multiple-input multiple-output receivers and artificial neural networks

Juan. A. Apolo<sup>1</sup>  | Isaac. N. O. Osahon<sup>2</sup> | Beatriz Ortega<sup>1</sup> | Vicenç Almenar<sup>1</sup> |  
Jianming Tang<sup>3</sup> | Sujan Rajbhandari<sup>4</sup>

<sup>1</sup>Instituto de Telecomunicaciones y Aplicaciones Multimedia, ITEAM, Universitat Politècnica de València, Valencia, Spain

<sup>2</sup>Electrical Engineering Division, University of Cambridge, Cambridge, UK

<sup>3</sup>DSP Centre of Excellence, School of Computer Science and Electronic Engineering, Bangor University, Bangor, UK

<sup>4</sup>Department of Physics, Institute of Photonics, University of Strathclyde, Technology & Innovation Centre, Glasgow, UK

**Correspondence**

Juan. A. Apolo.

Email: [juaapgon@teleco.upv.es](mailto:juaapgon@teleco.upv.es)

**Funding information**

Engineering and Physical Sciences Research Council, Grant/Award Number: EP/Y037243/1, TITAN Extension; European Cooperation in Science and Technology, Grant/Award Number: CA19111, NEWFOCUS; MCIN/AEI/10.13039/501100011033 and ERDF 'A way of making Europe', Grant/Award Number: PID2021-126514OB-I00 OPTIMIZE

**Abstract**

This paper proposes and presents the first experimental demonstration of a high-precision indoor 2D and 3D visible light positioning (VLP) system using an imaging multiple-input multiple-output (MIMO) configuration with supervised artificial neural network. The proposed system utilises four distributed transmitters and receiver with four photodiodes and an imaging optics. The experiments are conducted in a typical indoor environment with transmitter separations of 300 mm and a link distance of 1400 mm. The experimental results show 2D and 3D positioning accuracies of 3.7 and 51 mm, respectively. A simulation model is also developed for the VLP system to validate the experimental results. Further optimisation of the VLP system in the simulation platform leads to improved 2D and 3D positioning accuracies of 2 and 14.7 mm, respectively. The proposed system can be seamlessly integrated with existing lighting infrastructures and is also compatible with the MIMO visible light communication system, indicating the potential for practical implementation in integrated communications and positioning applications.

**KEYWORDS**

diversity reception, free-space optical communication, indoor communication, LED lamps, light transmission

## 1 | INTRODUCTION

Over the past decade, visible light communication (VLC) has emerged as a complementary technology to traditional radio frequency (RF)-based wireless communications for high-speed access networks. VLC leverages existing solid-state lighting infrastructure for high-speed wireless communication, thus offering advantages such as unlicensed spectrum operation, low power consumption, and cost-effective implementation [1]. Thus, VLC is expected to play a key role in upcoming 6G

networks, demonstrating high-speed transmission capabilities for aerial, submarine, and indoor networks and compatibility with various communication systems [2]. Among its many applications, indoor and outdoor visible light positioning (VLP) and navigation are promising areas.

Positioning technologies have recently attracted significant attention due to their applications in wide-ranging monitoring, surveillance, or tracking. Compared to RF positioning technologies, VLP offers unique advantages of high-accuracy due to shorter wavelengths and less sensitivity to multipath

This is an open access article under the terms of the [Creative Commons Attribution](https://creativecommons.org/licenses/by/4.0/) License, which permits use, distribution and reproduction in any medium, provided the original work is properly cited.

© 2025 The Author(s). *IET Optoelectronics* published by John Wiley & Sons Ltd on behalf of The Institution of Engineering and Technology.

propagation, zero electromagnetic interference (EMI), and dual functionalities of illumination and positioning [1].

VLP systems utilise photodiodes (PDs) or image sensors (IS) receivers to provide indoor positioning solutions. PD-based VLP systems offer advantages such as fast response times, compatibility with communications, and suitability for real-time applications and varying lighting conditions. Existing VLP techniques can be classified into two main categories: distance-based and distance-free [3, 4]. Distance-based techniques include the use of received signal strength (RSS) to estimate the distance between the receiver (Rx) and the transmitter (Tx) [5]. Other distance-based techniques employ time of arrival (TOA) [6] and time difference of arrival (TDOA) [7]; both require precise synchronisation between transmitters and receivers, resulting in increased system complexity. Furthermore, angle of arrival (AOA)-based techniques require diversified angles and a relatively large number of receiver devices to operate effectively [8]. Distance-free techniques are independent of geometric distance measurements but often require more complex hardware and configuration. One commonly adopted distance-free technique uses RSS values as fingerprint features for indoor positioning [9].

In contrast to PD-based VLP systems, IS-based VLP systems capture the images of the modulated intensity of LED luminaires and subsequently process them using image processing algorithms to estimate the position [10]. Most of these systems rely on complementary metal oxide semiconductor (CMOS) IS, which consists of a dense pixel grid optimised for capturing images. This architecture enables the extraction of detailed features, the improvement in interference rejection, and the mitigation of multipath reflections [11]. In contrast with CMOS-based IS, the imaging multiple-input multiple-output (MIMO) receiver employed in this work is based on an array of PDs combined with a lens system designed for high-speed communications and positioning. Furthermore, cameras are extensively incorporated into consumer devices, such as smartphones, enabling VLP systems to use existing hardware. However, these systems face inherent challenges for achieving high-speed communication due to frame rates constraints. While the techniques such as rolling shutter, associated with complementary metal-oxide-semiconductor (CMOS) sensor, can enhance data transmission rates, they remain constrained by factors such as the exposure time and electronic components used for signal processing. Furthermore, the number of symbols observed at the receiver is also influenced by the resolution of the image sensor, pixel clock, exposure time, and the size of the region of interest. These limitations, typically transmission speeds, are restricted to several kbps to a few Mbps [12], making such systems less suitable for high-speed communications and in certain scenarios.

Advanced solutions for improving VLP accuracy have been proposed based on machine learning and deep learning (ML/DL), that is, linear or higher-order regression [13]. Various algorithms, such as K-nearest neighbour (KNN), support vector machine, and artificial neural network (ANN) [14], are showcasing promising outcomes and achieving mm levels of accuracy. These techniques are often used in

fingerprint-based systems, where a database of RSS values and their corresponding coordinates is pre-collected. ANNs, for instance, are using offline fingerprint data. Once trained, ANNs can accurately predict a user's location in real-time based on new RSS measurements. The multi-layer perceptron (MLP) network, often configured with a single hidden layer, is a commonly chosen ANN architecture for conducting localisation tasks [15, 16].

The spatial diversity provided by multiple PDs improves the robustness of the positioning system against obstacles and interference, which are common challenges in indoor environments [17]. Moreover, the use of multiple PDs improves positioning accuracy, as detailed in Table 1. For example, tilted PDs were proposed to improve the accuracy of VLP systems [18], where a localisation error of 35 mm was obtained. Furthermore, a ML technique is combined with multiple detectors to provide higher accuracy. In ref. [19], four PDs and RSS-based fingerprinting with a weighted K-nearest neighbour (WkNN) algorithm were employed to demonstrate positioning errors of 8.3 and 20.45 mm with four and two luminaires, respectively. A VLP system based on a single LED and multiple silicon solar cells employing AOA and a long short-term memory neural network model has achieved an average positioning error of 17.8 mm, and 90% of the experimental data had a positioning error less than 29 mm [20]. Systems utilising angular diversity photodetectors or silicon solar cells prioritise the accuracy of positioning over the performance of communication. A theoretical approach based on 16 LED lamps and a grid of 361 receivers with three ANNs to estimate 3D positioning from RSS has achieved an average positioning error of 0.4 mm [21]. In ref. [22], a VLP system based on four evenly distributed LED emitters and a MLP achieved 2D positioning root-mean-square (RMS) errors of 10.3 and 13.3 mm for LOS and non-LOS links, and 3D localisation error of 19.8 and 21 mm. In ref. [23], the authors propose a deep residual shrinkage network with a single LED and 4-PDs, achieving 90% of positioning errors below 23.5 mm in simulations and below 100 mm in experiments.

The LiFi-based integrated communication and positioning paradigm is expected to be a key technology for 6G networks [24]. In VLC/LiFi technologies, numerous studies have shown high-speed communications utilising MIMO configurations and accurate VLP positioning facilitated by a distributed illumination infrastructure [25]. The optical MIMO receiver can be realised using imaging and non-imaging configurations [26]. Imaging MIMO systems are preferred over non-imaging MIMO configurations due to enhanced data rate scalability, compactness, and a well-conditioned channel H-matrix [26, 27]. These features not only improve communication performance but also make imaging MIMO systems particularly suited for dual functionality in communication and positioning applications. However, to the best of the authors' knowledge, there has been no previously published work demonstrating imaging MIMO configurations for highly accurate VLP. This paper is the first attempt to showcase highly accurate 2D/3D VLP using imaging MIMO setups. While this paper primarily focuses on proof-of-concept demonstrations of VLP using

**TABLE 1** Key experimental parameters for the imaging VLP system overview of diversity receiver-based VLP systems and original contribution of the proposed work.

Reference/ year	Technique	Type of study	Number of TxS	Number of PDs	Room dimensions	Compatible with 3D	Accuracy @90% CDF
					(mm × mm × mm) L × W × H		
[17], 2018	RSS	Simulation	1	4	3000 × 3000 × 1250	No No	35.0 mm
[18], 2021	RSS fingerprinting with fabricated data and ML	Experimental	4	4	1200 × 1200 × 1600	No No	8.3 mm
[19], 2022	AOA with LSTMNN	Experimental	1	4	400 × 400	No No	29.0 mm
[20], 2018	Three different ANNs (one for each axis)	Simulation	16	361 (19 × 19)	4000 × 4000 × 3000	Yes No	0.4 mm
[21], 2022	RSS fingerprinting (ML) ANN	Simulation	4	1–4	5000 × 5000 × 5000	Yes No	19.8 mm (LOS-3D)  10.3 mm (LOS-2D)
[22], 2024	Deep residual shrinkage network (DRSN)	Experimental & simulation	1	4	3600 × 3600 × 3000	Yes No	23.5 mm (simulation)  100 mm (experimental)
Our work	RSS fingerprinting MLP-ANN with imaging receiver	Experimental & simulation	4	4	410 × 410	Yes Yes	3.7 mm/51 mm (2D/3D, experimental)
					540 × 540 × 120		

such configurations, the overarching objective is to exhibit integrated communications and positioning in future iterations.

Hence, the novelty and original contributions of this paper are as follows:

- To the best of the authors' knowledge, this is the first experimental demonstration and simulation study of imaging optical MIMO configuration for 2D/3D positioning. Furthermore, this is the first study of utilising the supervised ANN with imaging MIMO for VLP.
- This paper provides a study of the impact of defocusing the lens at the receiver on VLP performance; clearly demonstrating the trade-off between the field of view (FOV) and positioning accuracy.
- This is the first experimental demonstration to verify the improved 2D and 3D positioning accuracy due to imaging spatial diversity provided by multiple PDs.
- This work demonstrates the potential of imaging MIMO VLP configuration for integrated sensing and communication applications, aligning with future 6G network requirements.

The subsequent sections of this work are organised as follows: Section 2 provides a detailed description of the proposed VLC positioning system, including the experimental setup and the signal processing for the ANN algorithm. Section 3 presents the results obtained from both laboratory measurements and simulations evaluating the accuracy of the 2D/3D positioning system. Finally, Section 4 presents the

conclusions of this work by summarising the feasibility and accuracy of the proposed 2D/3D VLP system and identifying the main challenges for further research.

## 2 | SYSTEM DESCRIPTION AND EXPERIMENTAL SETUP

Figure 1a depicts the experimental setup of the proposed VLP system, including the Tx and Rx configurations, the signal processing procedure at the Rx, and position estimation based on ANN, which will be described in detail in this section. The experimental parameters are summarised in Table 2. Similar to imaging MIMO-VLC systems [28, 29], the proposed VLP system employs a 4 × 4 imaging MIMO configuration that utilises white LEDs as TxS and an Rx with a PD array, and imaging optics.

### 2.1 | Transmitter

The VLP system utilises four symmetrically distributed TxS, spaced 300 mm apart, serving as illumination sources and signal transmitters for position estimation. Each transmitter comprises an LED (Samsung LM561C) and a reflector (LEDiL EMILY-W), producing a 40° beam divergence. The LED operates with an average bias current of 75 mA, creating a luminous flux of 46 lumens. Modulating signals are generated by four arbitrary waveform generators (AWGs), whose outputs

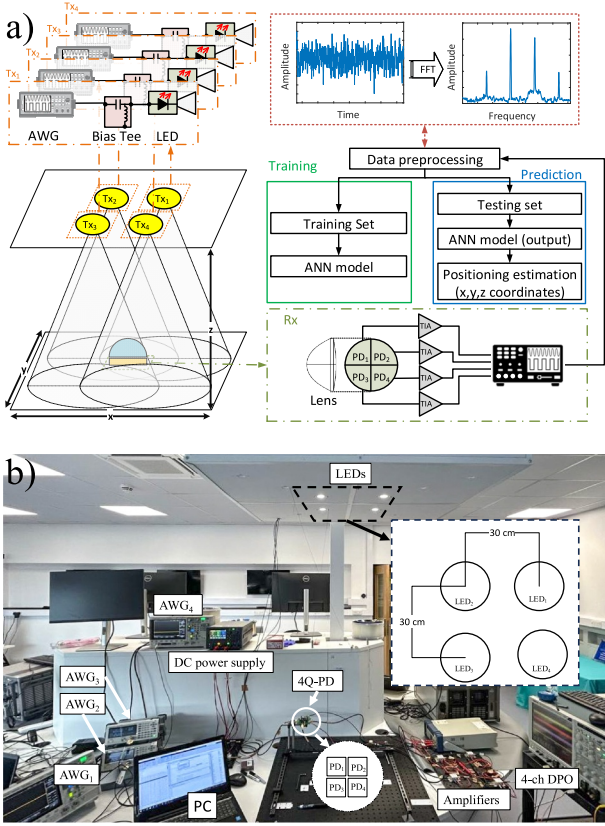


**FIGURE 1** Multi-PD visible light positioning system with an imaging receiver: (a) schematic diagram; (b) photograph of the laboratory setup. The insets show the geometrical distribution of the transmitters and receivers.

are converted into unipolar signals adding DC voltages using bias-Tees (MINI-CIRCUITS, ZFBT-4R2GW-FT+). Thus, a non-negative amplitude of the signal is ensured to modulate the intensity of each LED.

## 2.2 | Receiver

The imaging MIMO VLP configuration employs a plano-convex aspheric singlet lens (THORLABS, ACL2520U) with a 25 mm diameter and a 20.1 mm focal length as the imaging optics. A PD array with four individually addressable elements is used as the Rx, as shown in Figure 1. As stated in ref. [30], the FoV can be improved by defocusing (i.e. placing receivers at the offset distance ( $f_{\text{offset}}$ ) towards the lens from the focal plane) instead of placing the receiver at the focal plane. Then, the receiver can achieve a wider FoV to support improved localisation while maintaining a sufficient signal-to-noise ratio (SNR) for a reliable positioning operation. Hence, we utilised the focal offset ( $f_{\text{offset}}$ ) of 4 mm, providing a FoV of  $37.5^\circ$ , which closely matches the transmitter beam divergence of  $40^\circ$ . The signal output from each PD is independently amplified by a trans-impedance amplifier (TIA) (MAX3665) followed by a low-noise amplifier (LNA) with a 20-dB gain (MINI-CIRCUITS, ZFL-1000LN+). A 4-channel digital oscilloscope captures the signal, with each channel corresponding to each

**TABLE 2** Key experimental parameters for the imaging VLP system.

	Parameter	Value
LED		SAMSUNG LM561C
	Bias current $I_b$	75 mA
	Bias voltage $V_{DC}$	3.3 V
	Flux	43 lm @75 mA
Reflector		LEDiL CA11934_EMILY-W
	External diameter	$\varnothing$ 26 mm
	FWHM	$40^\circ$
RX lens		Thorlabs ACL2520U-A
	Diameter	$\varnothing$ 25 mm
	Focal length $f_c$	20.1 mm
	Back focal length $f_b$	12mm
PD		First sensor QP5.8-6-TO5
	Number of elements	4
	Active area of each PD	$1.44 \text{ mm}^2$
	Responsivity	0.4 A/W @632 nm
	Element gap	50 $\mu\text{m}$
	Amplifier	Mini-circuits ZFL-1000LN+
	Gain	19.9 dB
	Noise Figure	2.9 dB
		General
	Discrete frequencies	200, 400, 600, and 800 kHz
	No. of transmitters, $M_{Tx}$	4
	No. of receivers, $N_{Rx}$	4
2D	Test area	$410 \times 410 \text{ mm}^2$
	Link distance	1400 mm
3D	Test volume	$540 \times 540 \times 120 \text{ mm}^3$
	Link distance	1280–1400 mm

amplified PD output, followed by offline processing. The maximum SNR in our setup is measured as 51.9 dB.

## 2.3 | VLP channel

For the MIMO configuration with  $N_{Tx}$  transmitters and  $M_{Rx}$  receivers, the received signal can be calculated as follows:

$$\mathbf{S} = \mathbf{H}\mathbf{X} + \mathbf{n}; \quad (1)$$

where  $\mathbf{H}$  is the  $N_{Tx} \times M_{Rx}$  channel matrix;  $\mathbf{X}$  is the  $N_{Tx} \times 1$  transmitted signal vector;  $\mathbf{n}$  is the  $M_{Rx} \times 1$  noise vector and  $\mathbf{S}$  is the  $M_{Rx} \times 1$  received signal vector. Note that for the imaging optical MIMO communication system,  $M_{Rx} \geq N_{Tx}$ .

However, such a requirement is not necessary for the VLP-only applications, though a higher number of Rx improves the positioning accuracy, as detailed in Section 3. The channel gain from each  $Tx$  to each  $Rx$ , known as the channel  $\mathbf{H}$ -matrix, is given by

$$\mathbf{H} = \begin{bmatrix} b_{11} & b_{12} & \dots & b_{1N_{Tx}} \\ b_{21} & b_{22} & \dots & b_{2N_{Tx}} \\ \vdots & \vdots & \ddots & \vdots \\ b_{M_{Rx}1} & b_{M_{Rx}2} & \dots & b_{M_{Rx}N_{Tx}} \end{bmatrix}; \quad (2)$$

where  $b_{ij}$  is the channel gain from the  $j$ th transmitter to the  $i$ th receiver element. For the line-of-sight (LOS) link with Lambertian emission, the channel gain from the  $j$ th transmitter to  $i$ th receiver is given by

$$b_{ij} = \begin{cases} \frac{(m+1)A_{PD}}{2\pi d_{ij}^2} \cos^m(\phi_{ij}) T_s(\psi_{ij}) g(\psi_{ij}) \cos(\psi_{ij}) & 0 \leq \psi_{ij} \leq \psi_{FOV} \\ 0 & \text{Otherwise.} \end{cases} \quad (3)$$

where  $m = \frac{-1}{\log_2(\cos \Phi_{1/2})}$  is the Lambertian order,  $A_{PD}$  is the active area of the photodiode,  $d_{ij}$  is the distance between the transmitter and the receiver,  $\phi_{ij}$  is the radiance angle of the transmitter,  $\psi_{ij}$  is the angle of incidence with respect to the axis normal to the receiver surface,  $T_s$  is the filter transmission coefficient, and  $g$  and  $\psi_{FOV}$  are the concentrator gain and FOV, respectively. The optical concentrator gain at the receiver is given by

$$g(\psi_{ij}) = \begin{cases} \frac{n^2}{\sin^2 \psi_{ij}} & 0 \leq \psi_{ij} \leq \psi_{FOV}; \\ 0 & \text{Otherwise.} \end{cases} \quad (4)$$

where  $n^2$  is the refractive index of the optical concentrator. The channel gain information is related to RSS and can be used for positioning estimation. In line with other experimental VLP work [13], we have employed frequency division multiplexing (FDM) with four discrete frequencies to distinguish the signals from individual LEDs instead of time division multiplexing (TDM), where a low-frequency sinusoid signal is transmitted in a time sequence from each transmitter [28]. Such frequencies generated by AWGs ensure that each transmitter is uniquely identified, enabling their effective separation during pre-processing. The amplified photodiode signals are captured using an oscilloscope and sent to MATLAB, where fast Fourier transform (FFT) is applied to decompose the composite signal and extract the individual RSS values. The FFT is applied to

the received signal to compute the RSS corresponding to each transmitter. This operation is necessary to separate the FDM signals from multiple transmitters and prepare the inputs to the ANN for further processing.

## 2.4 | Artificial neural network model

As shown in Figure 2, a fully connected feedforward back-propagation supervised MLP ANN with one input layer, one hidden layer, and one output layer is implemented for 2D/3D positioning estimation. The number of neurons in the input layer equals  $M_{Rx} \times N_{Tx}$  corresponding to the channel  $\mathbf{H}$ -matrix for a particular position in Equation (2). The output layer has a linear transfer function with two/three neurons corresponding to 2D/3D positioning, respectively. A detailed

description of the ANN structure and corresponding training algorithm, including the optimisation process for the hidden layer, can be found in ref. [22]. Based on the optimisation, the hidden layer has 32 neurons with a sigmoid transfer function. The sigmoid transfer function is selected for its capacity to introduce non-linearities into the model, enabling the network to learn from the training data. The dataset used to train the ANN containing different RSS matrices paired with their corresponding positions is used to train the ANN, which jointly represents the spatial distribution of RSS and their variations due to the relative positions of the transmitters and receivers. During training, the network adjusts its weights to minimise errors between the estimated and actual positions. This is achieved by backpropagation, where the error gradient is propagated backward through the network, allowing the optimisation of the neural network parameters [31]. While various algorithms can be used with backpropagation to update the weights and biases of the MLP-ANN, we specifically use the Levenberg–Marquardt algorithm due to its superior convergence speed and minimal epoch requirements compared to alternative methods [32].

## 3 | RESULTS AND DISCUSSION

### 3.1 | Experimental results

The experiment aimed to evaluate the accuracy of the proposed 2D/3D positioning system by conducting measurements

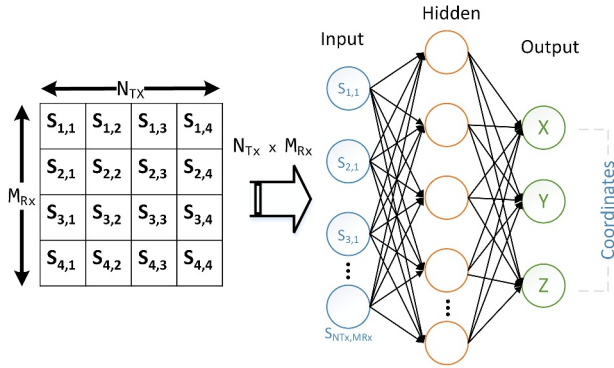


**FIGURE 2** Schematic diagram of artificial neural network model for visible light positioning.

within the predefined areas. The important experimental parameters are summarised in Table 2.

### 3.1.1 | 2D VLP

A grid of 2D points with a geometric spacing of 15 mm was created to evaluate the positioning accuracy. This geometric spacing was chosen to balance a detailed spatial analysis with the practical constraints of measurement time. Hence, by measurements, we collected 784 points within a  $410 \times 410 \text{ mm}^2$  area and a distance between the ceiling and the detector plane fixed at 1400 mm. The area under the test is chosen to have a representative coverage for the proof-of-concept demonstrations while still keeping a reasonable amount of data for training and testing. The system was evaluated based on the geometrical error's cumulative distribution function (CDF). Unless otherwise specified, we will use a CDF of 0.9 to specify the positioning error throughout the paper.

Figure 3a shows the empirical CDF of the positioning error for different numbers of ANN training data. Note that training is performed offline before the VLP system operation, so no real-time constraints are imposed in the proposed approach. Training ANN with 80% of the dataset (627 points) resulted in a positioning error of 3.7 mm. Conversely, reducing the number of training data to 60%, 40%, and 20% of the dataset resulted in positioning errors of 4.9 mm, 12.6 mm, and 31.6 mm, respectively. Figures 3b, c present the spatial distributions of errors across the test area. The figures compare the actual locations (denoted by crosses) with the locations estimated by the proposed system (represented by points). In Figure 3b, 627 training points were employed, and a smaller spread of the estimated positions around the actual positions is observed, indicating a higher overall positioning accuracy. In comparison, Figure 3c shows the results when 157 training points were used, representing 20% of the dataset. This figure shows a sparser distribution of estimated positions, reflecting the degradation in system performance due to the smaller training dataset size.

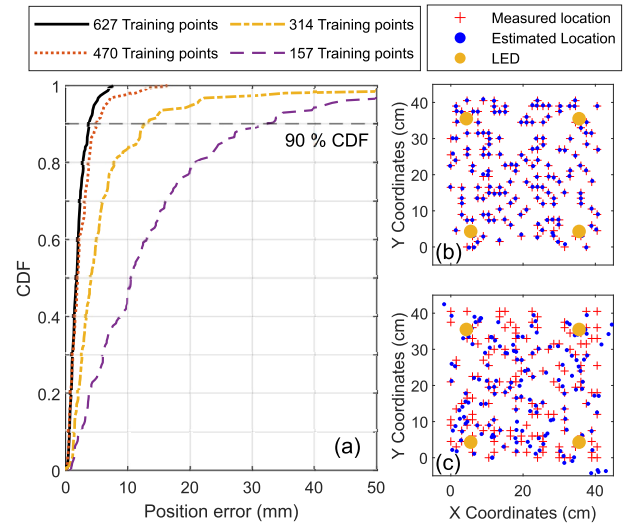


**FIGURE 3** (a) Cumulative distribution function of geometrical error of the proposed 2D visible light positioning system using different numbers of training points. Location of the measured and estimated points by the artificial neural network algorithm using different numbers of points: (b) 627 and (c) 157.

### 3.1.2 | 3D VLP

To assess the 3D positioning accuracy, measurements were conducted within a  $540 \times 540 \times 120 \text{ mm}^3$  volume to validate the proposed system as a proof-of-concept. The link distance of 1400 mm was considered as the base and was varied by moving the detector plane up to 120 mm closer to the ceiling (i.e. the transmitter–receiver distance ranged from 1400 to 1280 mm). The grid is structured by points spaced 30 mm apart, with 361 points for each 2D plane and five different vertical levels, that is, five 2D planes spaced 30 mm apart. The dataset comprises 1805 measurement points, 80% of which were used to train the ANN, and the remaining 20% were used to test and validate the algorithm.

Figure 4 shows the geometric error in the  $x$ -,  $y$ - and  $z$ -planes, as well as the combined 3D error, for both experimental (dashed lines) and simulation results (solid lines). The positioning accuracies in the  $x$ - and  $y$ -planes are comparable, where the error is close to 15 mm. As expected, the accuracy in  $x$ - and  $y$ -planes is similar to the value in 2D positioning experiments presented in Figure 3 for a similar number of training points (314). In contrast, the  $z$ -plane has a significantly higher error of  $\sim 51 \text{ mm}$ . This difference in error between the dimensions is due to the reduced number of training points in the  $z$ -plane, which results in lower positioning accuracy. The inset in Figure 4 visually compares 30 test points (crosses) and the estimated positions (dots) in that plane.

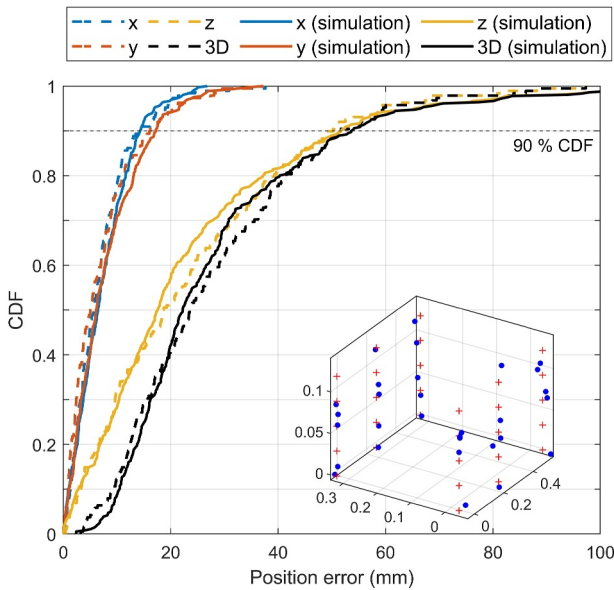
### 3.1.3 | Impact of number of receivers

Figure 5 demonstrates the impact of the receiver diversity on the accuracy of 2D and 3D positioning. In the case of 2D positioning, the positioning errors are 30 mm, 6 mm, 5 mm,

and 3.7 mm for one, two, three, and four PDs, respectively (see Figure 5a). Similarly, Figure 5b shows that the 3D positioning errors are 78 mm, 61 mm, 60 mm, and 51 mm for one, two, three, and four PDs, respectively. This clearly illustrates the advantage of a PD array receiver system with imaging optics in enhancing positioning accuracy. We anticipate further enhancements in 3D positioning by increasing the number of training points along the z-plane, as shown in the following section.

### 3.2 | Simulation results

The ZEMAX OpticStudio software is employed to verify and further extend the experimental results. The simulation



**FIGURE 4** Cumulative distribution function of geometrical error of the proposed 3D visible light positioning system, including the detail of individual  $x$ -,  $y$ -, and  $z$ -plane in the 3D positioning. Solid lines represent the simulation model. The inset shows the 3D scatter plot of the test and estimated positioning points.

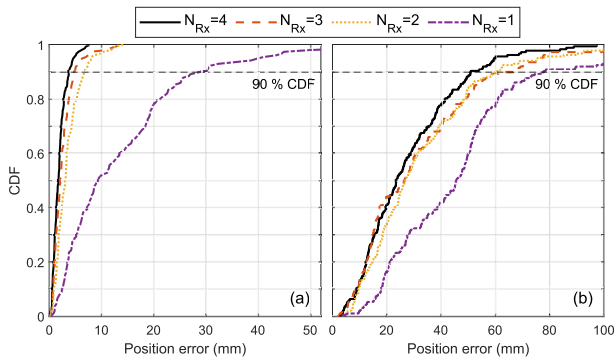


**FIGURE 5** Cumulative distribution function of the geometrical error of the proposed VLP system with different diversity orders  $N_{Rx} = 1-4$  for: (a) 2D VLP and (b) 3D VLP. VLP, visible light positioning.

scenarios replicate the experimental configurations and components described in the previous section, whereas optical powers and shot noise are adjusted to match the laboratory measurement conditions. As described in ref. [29], there is gain-FoV trade-off, and hence the imaging optics system was optimised by varying  $f_{offset}$ , that is, distance of the lens from its focal point towards the detectors to modify the size of the image formed at the receiver and to study the impact on positioning accuracy.

Figure 6a presents the CDF of the positioning error of the 2D-VLP system for  $f_{offset}$  ranging from 0 to 6 mm. As in the case of experimental work, 80% of the dataset is used to train the ANN, and the remaining 20% is used for testing. The solid line represents the CDF obtained from laboratory measurements, showing excellent agreement with simulation results, with a positioning error of 3.7 mm at  $f_{offset} = 4$  mm. This correspondence validates the accuracy of the simulation model in replicating the experimental setup, allowing further extension of the experimental findings. The positioning error initially decreases with increasing  $f_{offset}$ , reaching a minimum error of approximately 2.6 mm at  $f_{offset} = 2$  mm; beyond this point, the error begins to increase. For instance, the positioning errors for  $f_{offset}$  of 3 and 4 mm are  $\sim 2.9$  and 3.5 mm, respectively.

Figures 6b–d show the spatial distributions of the geometric error for an offset of 4 mm, 2 mm, and 0 mm, respectively. Figures 6b,c reveal a relatively uniform

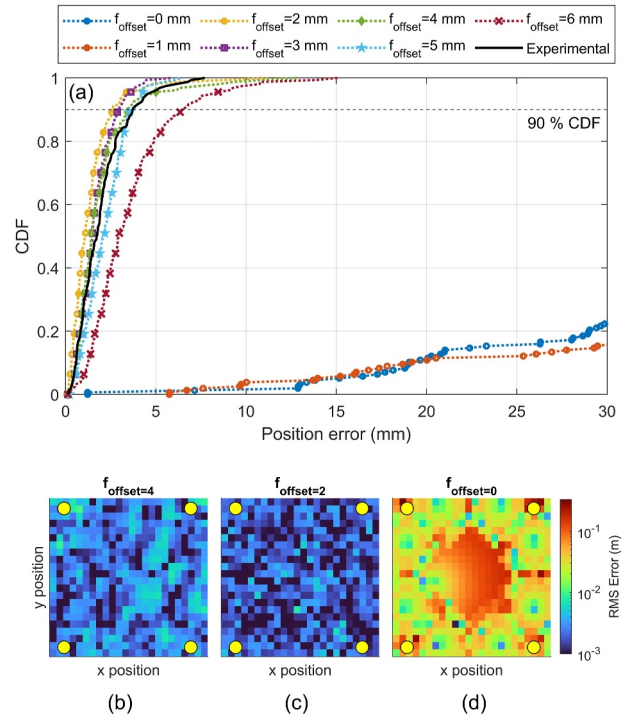


**FIGURE 6** (a) Cumulative distribution function of geometrical error from simulations for different focal offsets between the lens and the photodetectors (black curve corresponds to experimental results). Spatial distribution of the geometrical error for: (b)  $f_{offset} = 4$  mm (c)  $f_{offset} = 2$  mm and (d)  $f_{offset} = 0$  mm. The yellow circles represent the location of the four transmitters.

distribution of positioning errors across the measured area. In contrast, Figure 6d corresponding to  $f_{\text{offset}} = 0$  mm shows a notable variation in error distribution, with certain regions exhibiting significantly higher errors, particularly in the centre. These areas of increased error are due to lower received signal intensity, as the image of Tx does not fall into any of the PDs due to narrow FoV (discussed further below).

Figure 7 provides a further analysis of the imaging MIMO VLP system. The simulation of the spatial intensity distribution (incoherent irradiance  $\text{W}/\text{m}^2$ ) depicts the received optical intensity at the image plane. The red lines represent the PD array in the image plane. The first row (Figures 7a–c) depicts the images formed when the detector is located at the geometrical centre formed by the transmitters. The second row (Figures 7d–f) represents the images formed when the receiver is positioned directly below one of the transmitters. Each column represents a  $f_{\text{offset}}$  of 4 mm, 2 and 0 mm (from left to right). As observed, the focal offset significantly impacts the spatial distribution of intensity. The clearest image is formed when the receiver plane is at the focal point ( $f_{\text{offset}} = 0$  mm). However, the images from the transmitters are outside the PDs, significantly reducing the received power. On the other hand, at  $f_{\text{offset}} = 4$  mm, the images formed from the transmitters overlap significantly and are difficult to distinguish (this overlap leads to substantial inter-channel interference, resulting in a higher condition number for the MIMO  $\mathbf{H}$ -matrix). In contrast,  $f_{\text{offset}} = 2$  mm proves to be the optimal configuration, showing a clearly separated image from the four transmitters. Hence, as in the case of the imaging MIMO-VLC system [31], the condition number of channel  $\mathbf{H}$ -matrix affected the positioning accuracy, and optimisation of the optic system is necessary to obtain the best condition number.

Furthermore, the impact of SNR on the VLP performance is shown in Figure 8, where the position accuracy has been estimated for the best-case configuration  $f_{\text{offset}} = 2$  mm under

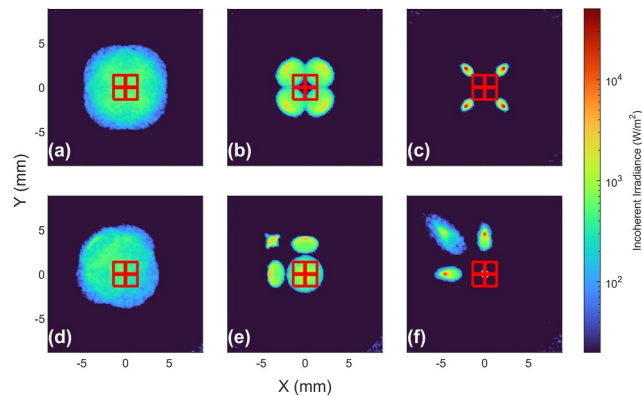


**FIGURE 7** Simulation of the image formed by the transmitters at the detector plane for different  $f_{\text{offset}}$  and different locations. First row: The receiver is at the geometrical centre of the four transmitters and  $f_{\text{offset}}$  is (a) 4 mm, (b) 2 mm, and (c) 0 mm. Second row: The receiver is located directly under one of the transmitters and  $f_{\text{offset}}$  is (d) 4 mm, (e) 2 mm, and (f) 0 mm. The red lines represent the PD array of four elements at the imaging plane.

an SNR range of 25–60 dB. As expected, the accuracy of the system decreases as the SNR decreases. In particular, the accuracy decreases from  $\sim 2$  to  $\sim 16.9$  mm when the maximum SNR reduces from 60.9 to 25.9 dB. However, the SNR has only a marginal impact on the positioning at high SNR, for example, position accuracy decreases from 2 to 2.4 mm when SNRs are 60.9 and 50.9 dB, respectively. The insets illustrate the SNR distribution over the measurement area for a single transmitter and a single PD from the array. Note the significant drops in SNRs towards the edge of coverage areas.

Finally, simulations for 3D positioning were carried out in an enlarged volume of  $540 \times 540 \times 240$  mm<sup>3</sup> under the same configuration as employed in the laboratory ( $f_{\text{offset}} = 4$  mm) for estimating the potential accuracy of the experimental 3D positioning system with a larger number of dataset points. The simulation grid is structured by points spaced 15 mm apart in the horizontal and vertical dimensions. This configuration results in a total of 1369 points in each of the 2D planes. The grid was divided vertically into 17 different levels ( $\pm 120$  mm from the 2D level); thus, the simulation dataset comprises 23273 points for 3D. As in all other cases, 80% of the dataset (18618) is used to train the ANN, and the remaining 20% is used for testing (4655). Figure 9 displays the CDF of the 3D positioning along the  $x$ -,  $y$ - and  $z$ -planes, as well as the combined total positioning error.

The  $x$ - and  $y$ -planes errors are similar and relatively low, with positioning errors of  $\sim 5.9$  mm. The  $z$ -plane, on the other hand, exhibits a greater error of 13.5 mm. The total 3D positioning error, which combines the errors of all three axes,

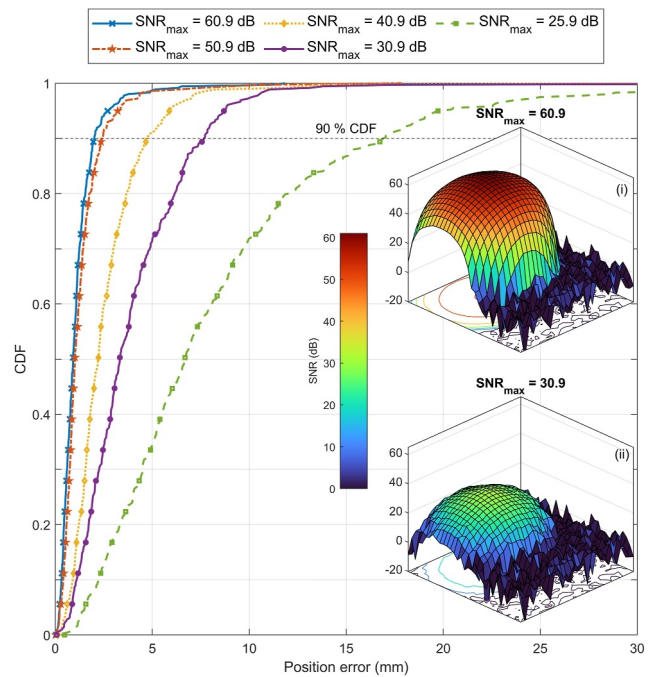


**FIGURE 8** Cumulative distribution function of the geometric error from simulations with a configuration of  $f_{\text{offset}} = 2$  mm and 1513 dataset points for different SNR = 60.9–25.9 dB. Insets show the SNR distribution within the measurement area for one LED and one PD from the array for the best-case scenario of: (i) 60.9 dBm and (ii) 30.9 dBm.



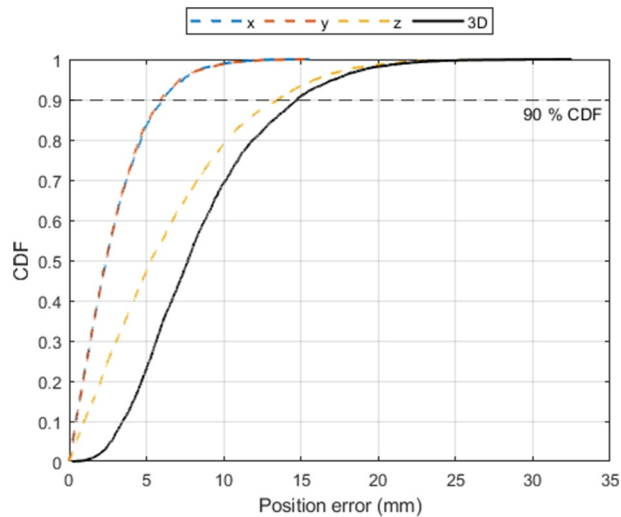


**FIGURE 9** Cumulative distribution function of the geometrical error for 3D visible light positioning from simulations with a configuration of  $f_{\text{offset}} = 4$  mm and 23273 dataset points.

is 14.7 mm, which is significantly lower than the experimental results of 51 mm. This improvement is due to the higher density of training points in the z-plane in the simulation, which allows for a more accurate representation of the measurement space and shows the potential of our approach for further improvement under larger training schemes.

## 4 | CONCLUSIONS

This paper presents an experimental demonstration of a high-accuracy 2D and 3D VLP system using an optical imaging MIMO system with supervised ANN. Experimental results show the impact of the number of training points and the spatial diversity on positioning accuracy, leading to 3.7 and 51 mm for 2D and 3D positioning accuracy, respectively.

The experimental work is validated and further extended by simulations. The simulation results allow to estimate the required number of training points and evaluate the impact of the system noise. Furthermore, the study underscores the critical role of optimising the imaging optics, particularly the focal offset, in achieving high-accuracy positioning. Using the experimental parameters under an optimised system configuration, the simulations results demonstrated a 2D positioning error of 2.6 mm, that can be reduced to 2.0 mm with 10 dB higher SNR. For 3D positioning, simulations employing experimental parameters over an extended volume show an error of 14.7 mm. Therefore, high-accuracy 2D/3D positioning has been demonstrated in a scalable imaging MIMO configuration as a promising solution for integrated positioning and communications applications. These advantages lead to the proposed VLP imaging MIMO system as a promising solution for future 6G networks requiring high-precision indoor positioning capabilities.

## AUTHOR CONTRIBUTIONS

**Juan. A. Apolo:** Formal analysis; investigation; software; writing—original draft; writing—review & editing. **Isaac. N. O. Osahon:** Investigation; software; writing—review & editing. **Beatriz Ortega:** Formal analysis; funding acquisition; supervision; validation; writing—review & editing. **Vicenç Almenar:** Formal analysis; supervision; validation; writing—review & editing. **Jianming Tang:** Formal analysis; funding acquisition; project administration; resources; writing—review & editing. **Sujan Rajbhandari:** Conceptualisation; formal analysis; methodology; software; supervision; visualization; writing—review & editing.

## ACKNOWLEDGEMENTS

This work has been supported by COST action CA19111 (NEWFOCUS). It has also been funded by Grant PID2021-126514OB-I00 optimise by MCIN/AEI/10.13039/501100011033 and ERDF ‘A way of making Europe’. SR and JT acknowledge support by the UK Engineering and Physical Sciences Research Council under Grant EP/Y037243/1 (TITAN Extension).

## CONFLICT OF INTEREST STATEMENT

The authors declare no conflicts of interest.

## DATA AVAILABILITY STATEMENT

The data that support the findings of this study are available from the corresponding author upon reasonable request.

## ORCID

Juan. A. Apolo  <https://orcid.org/0000-0002-7236-4968>

## REFERENCES

- Chen, P., et al.: A survey on visible light positioning from software algorithms to hardware. *Wireless Communications and Mobile Computing* 2021(1), 9739577 (2021). <https://doi.org/10.1155/2021/9739577>
- Chi, N., et al.: Visible light communication in 6G: advances, challenges, and prospects. *IEEE Vehicular Technology Magazine* 15(4), 93–102 (2020). <https://doi.org/10.1109/mvt.2020.3017153>
- Tran, H.Q., Ha, C.: Machine learning in indoor visible light positioning systems: a review. *Neurocomputing* 491, 117–131 (2022). <https://doi.org/10.1016/j.neucom.2021.10.123>
- Luo, J., Fan, L., Li, H.: Indoor positioning systems based on visible light communication: state of the art. *IEEE Commun. Surv. Tutorials* 19(4), 2871–2893 (2017). <https://doi.org/10.1109/comst.2017.2743228>
- Du, P., et al.: Experimental demonstration of 3D visible light positioning using received signal strength with low-complexity trilateration assisted by deep learning technique. *IEEE Access* 7, 93986–93997 (2019). <https://doi.org/10.1109/access.2019.2928014>
- Akiyama, T., Sugimoto, M., Hashizume, H.: Time-of-arrival-based smartphone localization using visible light communication. In: 2017 International Conference on Indoor Positioning and Indoor Navigation (IPIN), pp. 1–7 (2017)
- Du, P., et al.: Demonstration of a low-complexity indoor visible light positioning system using an enhanced TDOA scheme. *IEEE Photonics Journal* 10(4), 1–10 (2018). <https://doi.org/10.1109/jphot.2018.2841831>
- Steendam, H.: A 3-D positioning algorithm for AOA-based VLP with an aperture-based receiver. *IEEE J. Select. Areas Commun.* 36(1), 23–33 (2018). <https://doi.org/10.1109/jsac.2017.2774478>

9. Wei, F., et al.: Accurate visible light positioning technique using extreme learning machine and meta-heuristic algorithm. *Optics Communications* 532, 129245 (2023). <https://doi.org/10.1016/j.optcom.2022.129245>
10. Yang, Y., et al.: Positioning using wireless networks: applications, recent progress and future challenges. *IEEE Journal on Selected Areas in Communications* 42(9), 2149–2178 (2024). <https://doi.org/10.1109/jsac.2024.3423629>
11. Zhu, Z., et al.: A survey on indoor visible light positioning systems: fundamentals, Applications, and Challenges (2024)
12. Bastiaens, S., et al.: Visible light positioning as a next-generation indoor positioning technology: a tutorial. *IEEE Commun. Surv. Tutorials* 26(4), 2867–2913 (2024). <https://doi.org/10.1109/comst.2024.3372153>
13. Wu, Y.-C., et al.: Received-signal-strength (RSS) based 3D visible-light-positioning (VLP) system using Kernel ridge regression machine learning algorithm with sigmoid function data preprocessing method. *IEEE Access* 8, 214269–214281 (2020). <https://doi.org/10.1109/access.2020.3041192>
14. He, J., et al.: Demonstration of high precision 3D indoor positioning system based on two-layer ANN machine learning technique. In: *Optical Fiber Communication Conference (OFC) 2019*. OSA, San Diego (2019). Th31.2
15. Zafari, F., Gkelias, A., Leung, K.K.: A survey of indoor localization systems and technologies. *IEEE Commun. Surv. Tutorials* 21(3), 2568–2599 (2019). <https://doi.org/10.1109/comst.2019.2911558>
16. Liu, H., et al.: Survey of wireless indoor positioning techniques and systems. *IEEE Trans. Syst., Man, Cybern. C* 37(6), 1067–1080 (2007). <https://doi.org/10.1109/tsmcc.2007.905750>
17. Wang, K., Tan, H.: Positioning algorithm based on space constraint of the PD array in VLP system. *Optics Communications* 561, 130510 (2024). <https://doi.org/10.1016/j.optcom.2024.130510>
18. Yu, X., Wang, J., Lu, H.: Single LED-based indoor positioning system using multiple photodetectors. *IEEE Photonics J* 10(6), 1–8 (2018). <https://doi.org/10.1109/jphot.2018.2848947>
19. Bakar, A.H.A., et al.: Accurate visible light positioning using multiple-photodiode receiver and machine learning. *IEEE Trans. Instrum. Meas.* 70, 1–12 (2021). <https://doi.org/10.1109/tim.2020.3024526>
20. Hsu, L.-S., et al.: Utilizing single light-emitting-diode (LED) lamp and silicon solar-cells visible light positioning (VLP) based on angle-of-arrival (AOA) and long-short-term-memory-neural-network (LSTMNN). *Optics Communications* 524, 128761 (2022). <https://doi.org/10.1016/j.optcom.2022.128761>
21. Alonso-González, I., et al.: Discrete indoor three-dimensional localization system based on neural networks using visible light communication. *Sensors* 18(4), 4 (2018). <https://doi.org/10.3390/s18041040>
22. Mahmoud, A.A., et al.: Precision indoor three-dimensional visible light positioning using receiver diversity and multi-layer perceptron neural network. *IET Optoelectronics* 14(6), 440–446 (2020). <https://doi.org/10.1049/iet-opt.2020.0046>
23. Li, S., et al.: Indoor positioning system for single LED light based on deep residual shrinkage network. *Optics Communications* 559, 130366 (2024). <https://doi.org/10.1016/j.optcom.2024.130366>
24. Li, J., et al.: Integrated communication and positioning for IRS-assisted LiFi networks. In: *2024 IEEE Wireless Communications and Networking Conference (WCNC)*, pp. 01–06. IEEE, Dubai, United Arab Emirates (2024)
25. Wang, R., et al.: Integrated mobile visible light communication and positioning systems based on decision feedback channel estimation. *Photonics* 11(6), 537 (2024). <https://doi.org/10.3390/photonics11060537>
26. Rajbhandari, S., et al.: A review of gallium nitride LEDs for multi-gigabit-per-second visible light data communications. *Semiconductor Science and Technology* 32(2), 023001 (2017). <https://doi.org/10.1088/1361-6641/32/2/023001>
27. Zeng, L., et al.: High data rate multiple input multiple output (MIMO) optical wireless communications using white led lighting. *IEEE J. Select. Areas Commun.* 27(9), 1654–1662 (2009). <https://doi.org/10.1109/jsac.2009.091215>
28. Azhar, A.H., Tran, T.-A., O'Brien, D.: A gigabit/s indoor wireless transmission using MIMO-OFDM visible-light communications. *IEEE Photon. Technol. Lett.* 25(2), 171–174 (2013). <https://doi.org/10.1109/lpt.2012.2231857>
29. Werfli, K., et al.: Experimental demonstration of high-speed 4 × 4 imaging multi-CAP MIMO visible light communications. *J. Lightwave Technol.* 36(10), 1944–1951 (2018). <https://doi.org/10.1109/jlt.2018.2796503>
30. Dehghani Soltani, M., et al.: High-speed imaging receiver design for 6G optical wireless communications: a rate-FOV trade-off. *IEEE Trans. Commun.* 71(2), 1024–1043 (2023). <https://doi.org/10.1109/tcomm.2022.3230954>
31. Rumelhart, D.E., Hinton, G.E., Williams, R.J.: Learning representations by back-propagating errors. *Nature* 323(6088), 533–536 (1986). <https://doi.org/10.1038/323533a0>
32. Hagan, M.T., Menhaj, M.B.: Training feedforward networks with the Marquardt algorithm. *IEEE Trans. Neural Netw.* 5(6), 989–993 (1994). <https://doi.org/10.1109/72.329697>

**How to cite this article:** Apolo, J.A., et al.: Experimental demonstrations of high-accuracy 3D/2D indoor visible light positioning using imaging multiple-input multiple-output receivers and artificial neural networks. *IET Optoelectron.* e70000 (2025). <https://doi.org/10.1049/ote2.70000>